

Joint Analysis of Regional Strain Variations Based on Borehole Strainmeter and Global Navigation Satellite System Observations

Junyi Fan, Lei Tang,* Yuebing Wang, Yu Li, and Gaochuan Liu

China Earthquake Networks Center, China Earthquake Administration, Beijing 100045, China

(Received October 25, 2022; accepted November 22, 2022; online published December 5, 2022)

Keywords: four-gauge borehole strainmeter, global navigation satellite system, Kalman filter, principal strain

Several different types of crustal deformation sensors have been deployed in mainland China and have produced a massive amount of crustal deformation data. By fusing the data from sensors with different frequencies, positions, depths, and precisions, the comprehensive characteristics of the overall regional deformation can be revealed. In this study, we used near-surface and surface deformation sensors for Xinzhou area, Shanxi Province, China, which include a four-gauge borehole strainmeter (FGBS) and a global navigation satellite system (GNSS) receiver at different depths, respectively, to analyze the deformation in the study area. A joint analysis of the principal strain time series was conducted through strain conversion, and it was found that the study area is currently in a stable compressive state. It is concluded that GNSS and FGBS sensors can be deployed at the same station to facilitate the 3D observation and collaborative analysis of surface and shallow surface deformation.

1. Introduction

A four-gauge borehole strainmeter (FGBS) as an *in situ* location sensor in multiple models of geosensors can detect 2D changes in horizontal strain. The probe is generally buried at a depth of tens to hundreds of meters to measure the strain variations near the surface, it is an important means of crustal deformation observation in mainland China.^(1,2) The probe is a sealed steel cylinder with a circular cross section and four sensors for measuring changes in the inner diameter. The instrument probe is placed in the borehole at a location with a hard and complete rock texture, and the space between the probe and the surrounding medium is filled with coupling cement (a mixture of cement and quartz sand prepared in a specific proportion in accordance with the rock properties of the measured section) that couples the instrument probe with the rock. FGBSs have been used to collect data in China for over 40 years and are currently a key way of collecting crustal deformation data in mainland China. There are currently more than 70 FGBS observation stations. These observations play an important role in earthquake

*Corresponding author: e-mail: TangLei06@seis.ac.cn
<https://doi.org/10.18494/SAM4198>

prediction in mainland China. In addition, borehole strain observations have been obtained in many other countries such as the United States and Japan. For example, borehole strain observations are an important part of the U.S. Public Benefits Outreach (PBO) Project.⁽³⁾ The Crustal Movement Observation Network of China began large-scale global navigation satellite system (GNSS) observations in 1999 and has carried out multiple measurements thus far.^(4,5)

The output of an FGBS is strain, which is a tensor; and the GNSS observations yield displacement data (including velocity and acceleration), which are vectors. Silver *et al.*⁽³⁾ analyzed postseismic deformation, slow earthquakes, and volcanoes in the San Andreas fault using observation data, and they determined the dominant frequency bands for the global positioning system (GPS), interferometric synthetic aperture radar (InSAR), pendulum seismometers, and borehole strain gauges. It was found that borehole strain observations and GNSS data are complementary in different frequency bands. Ohtani *et al.*⁽⁶⁾ compared the linear strains obtained from GNSS and borehole strain observations and found that the amplitudes of the linear strains of the GNSS and borehole strain observations were consistent at some measuring points. In addition, several researchers from China have conducted strain calculations based on borehole strain gauge observations,^(7–12) and they obtained strain parameters such as the additional principal strain and the principal strain direction. The same parameters can also be obtained from GNSS observations,^(13–15) providing a novel method for the joint analysis of strain variations using borehole strain gauge and GNSS observations. Two deformation observation instruments have produced a large amount of observation data, but the two observations have not been effectively combined and jointly analyzed.

In this study, using the analytical method of elasticity theory, we calculated parameters such as the principal strain direction, plane strain, and maximum shear strain from FGBS and GNSS observations. The variations in the principal strain at a point source near the surface due to tectonic activity were obtained from FGBS data. The variations in the regional surface strain were obtained from GNSS data. Using these data, we jointly analyzed the strain variations from the point source scale to the regional scale and from the surface to the near surface. The effectiveness of combining the two observation instruments with different sensors is then discussed on the basis of the research results, providing the basis and support for the future deployment of the two sensor instruments at the same station.

2. Data Analysis Methods

2.1 FGBS data analysis

When FGBSs were used to measure strain, relative and absolute calibrations of the observation data were first carried out. The coupling coefficients A and B were inverted to make appropriate corrections to the observation data. The FGBS were symmetrical, and the angle between two adjacent components was 45°. ⁽⁹⁾ The calculations of the four components using observed data are shown below.

$$\begin{aligned}
S_1 = S_{\theta_1} &= A(\varepsilon_1 + \varepsilon_2) + B(\varepsilon_1 - \varepsilon_2) \cos 2(\theta_1 - \varphi) \\
S_2 = S_{\theta_1 + \frac{\pi}{4}} &= A(\varepsilon_1 + \varepsilon_2) - B(\varepsilon_1 - \varepsilon_2) \sin 2(\theta_1 - \varphi) \\
S_3 = S_{\theta_1 + \frac{\pi}{2}} &= A(\varepsilon_1 + \varepsilon_2) - B(\varepsilon_1 - \varepsilon_2) \cos 2(\theta_1 - \varphi) \\
S_4 = S_{\theta_1 + \frac{3\pi}{4}} &= A(\varepsilon_1 + \varepsilon_2) + B(\varepsilon_1 - \varepsilon_2) \sin 2(\theta_1 - \varphi)
\end{aligned} \tag{1}$$

The principal strain, maximum shear strain, plane strain, and azimuth angle of the principal strain at a given observation point were calculated using^(1,7)

$$\begin{aligned}
S_{13} &= S_1 - S_3, \\
S_{24} &= S_2 - S_4, \\
S_a &= (S_1 + S_2 + S_3 + S_4) / 2,
\end{aligned} \tag{2}$$

$$\begin{aligned}
\varepsilon_1 &= \frac{1}{4A} S_a + \frac{1}{4B} \sqrt{S_{13}^2 + S_{24}^2}, \\
\varepsilon_2 &= \frac{1}{4A} S_a - \frac{1}{4B} \sqrt{S_{13}^2 + S_{24}^2}, \\
\varphi &= \frac{1}{2} \arctan \left(\frac{S_{24}}{S_{13}} \right) + \theta_1,
\end{aligned} \tag{3}$$

plane strain: $S_a = \varepsilon_1 + \varepsilon_2$; maximum shear strain: $S_s = \varepsilon_1 - \varepsilon_2$.

2.2 GNSS data analysis

Using GAMIT software, the coordinates of the observation stations in the land network were calculated using standard parameters and models. It was assumed that the crustal strain was uniform in the elements which are multiple tiny units divided from the research area and that each element had only one set of strain tensors (ε_{11} , ε_{22} , ε_{12}). Moreover, it was assumed that the rotation of the elements in each independent block was the same. The element strain tensor model was used to obtain the strain tensor of each element as well as the covariance matrix of the strain vectors. To simplify the calculations, the Gaussian covariance function was used to simulate the displacement variance–covariance matrix, and the maximum shear strain and plane strain of each element were calculated using⁽¹³⁾

$$\begin{aligned}
\varepsilon_1 &= \frac{1}{2}(\varepsilon_{11} + \varepsilon_{22}) + \frac{1}{2} \left[(\varepsilon_{11} - \varepsilon_{22})^2 + 4\varepsilon_{12}^2 \right]^{1/2}, \\
\varepsilon_2 &= \frac{1}{2}(\varepsilon_{11} + \varepsilon_{22}) - \frac{1}{2} \left[(\varepsilon_{11} - \varepsilon_{22})^2 + 4\varepsilon_{12}^2 \right]^{1/2}, \\
\theta_1 &= \frac{1}{2} \tan^{-1} \left(\frac{-2\varepsilon_{12}}{\varepsilon_{11} - \varepsilon_{22}} \right),
\end{aligned} \tag{4}$$

plane strain: $S_a = \varepsilon_1 + \varepsilon_2$; maximum shear strain: $S_s = \varepsilon_1 - \varepsilon_2$.

2.3 Fusion algorithm

The Kalman filter is one of the fusion methods based on estimation, and it involves feature-level fusion and has a wide range of applications in deformation data processing. It can produce accurate estimates of deformation trends. In this study, the Kalman filter was used to analyze the principal strain parameters obtained using multiple sensors in the study area.

If N types of sensors are used to monitor the deformation in the study area and the principal strain calculated from each sensor is L_k , then the matrix equation is⁽¹⁶⁾

$$L_k = B_k X_k + V_k. \quad (5)$$

If the estimated value of X is \hat{X} , the optimal estimated value can be obtained via least squares estimation as follows.

$$\begin{aligned} \hat{X}_{k,k} &= \hat{X}_{k,k-1} + \sum_{i=1}^N K_k^i (L_k^i - B_k^i \hat{X}_{k,k-1}) \\ P_{k,k}^{-1} &= P_{k,k-1}^{-1} + \sum_{i=1}^N \left[(B_k^i)^T (R^i)^T B_{k+1}^i \right] \\ \hat{X}_{k,k-1} &= \Phi_{k-1} \hat{X}_{k-1,k-1} \\ P_{k,k-1} &= \Phi_{k-1} P_{k-1,k-1} \Phi_{k-1}^T + \Gamma_k Q_k \Gamma_k^T \\ K_k^i &= P_k (B_{k+1}^i)^T (R_{k+1}^i)^{-1} \end{aligned} \quad (6)$$

3. Results

3.1 Study area

In this study, Xinzhou area, Shanxi Province, China, was chosen as the study area. According to the official earthquake catalogue of China Earthquake Networks Center, since 2015, this area has experienced 12 earthquakes of magnitude 3.0–3.9 and two earthquakes of magnitude 4.0–4.9 (both of magnitude 4.1 in 2016). There have been few earthquakes of magnitude 3 in this area since 2015. This area contained five sets of YRY-4 FGBSs and 20 sets of GNSS receivers, forming the dense regional observation network shown in Fig. 1. The distribution of the measuring points in the area was dense, resulting in high data quality, and the equipment was very stable. Thus, this was an ideal area for studying the characteristics of the regional strain field.

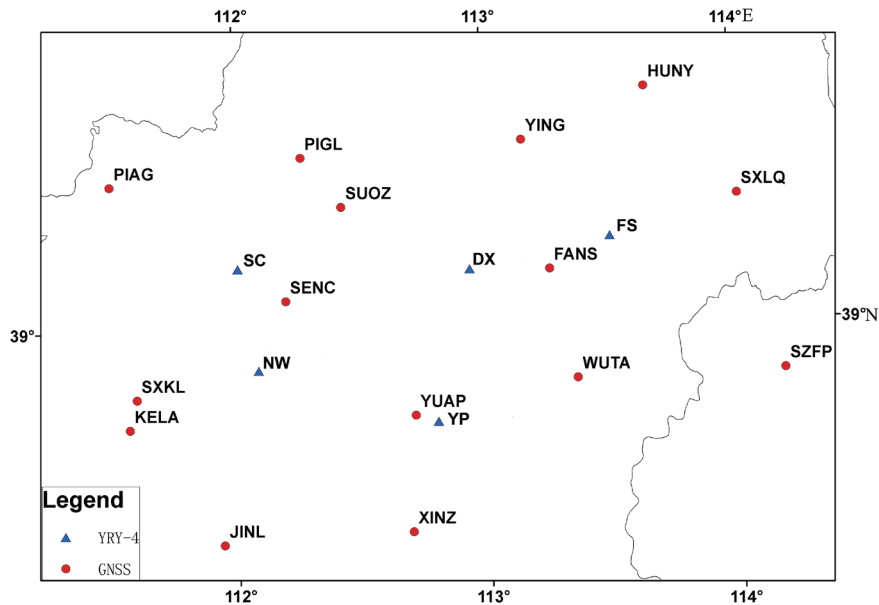


Fig. 1. (Color online) Distribution of YRY-4 and GNSS receivers in Xinzhou area, Shanxi Province.

3.2 Borehole strain data

The stress–strain state of the Xinzhou area was obtained using the FGBSs. Table 1 shows the specific numerical results of the main strain parameters at the FGBS station. In Fig. 2, the arrows indicate the direction and magnitude of the tensile and compressive strains obtained from the FGBS observations, and the red and blue arrows denote tension and compression, respectively. The figure shows that the southern segment of the Kouquan fault and the areas near the northern foot of the Hengshan fault were under tension and compression, dominated by NE-oriented tensile deformation. The eastern and southern parts of the Xinzhou area were mainly under compression, and the principal compressive stress in the northern section of the fault at the western foot of the Wutai Mountains was oriented toward the northwest. The southern section of the fault at the western foot of the Wutai Mountains and the western section of the Yunzhong Mountains were mainly under NE–E-oriented compressive stress. In summary, the Xinzhou area was predominantly under compressive stress, but there was a tension–compression transition area in the northern part of the study area.

3.3 GNSS data

Using the data from the 20 GNSS observation stations in the Xinzhou area, we calculated the regional velocity field (Eurasian framework).⁽¹⁷⁾ By considering the velocity field, we used the least squares method to calculate the maximum shear strain rate and the plane strain rate in the study area.^(13,15) The shear and plane strain rates are plotted in Fig. 3, where interpolation was used.⁽¹⁸⁾ The results revealed that the study area was dominated by compressive stress.

Table 1
Maximum shear strain rate, plane strain rate, and azimuth angle of principal strain obtained from five FGBSs.

Station	Maximum shear strain rate ($10^{-8}/a$)	Plane strain rate ($10^{-8}/a$)	Azimuth of main direction (unit: $^{\circ}$, north is 0° , and clockwise is positive)
DX	21	5.4	17
YP	0.56	-1	134
NW	1.5	-9	-19
FS	16	-60	70
SC	12	12	14

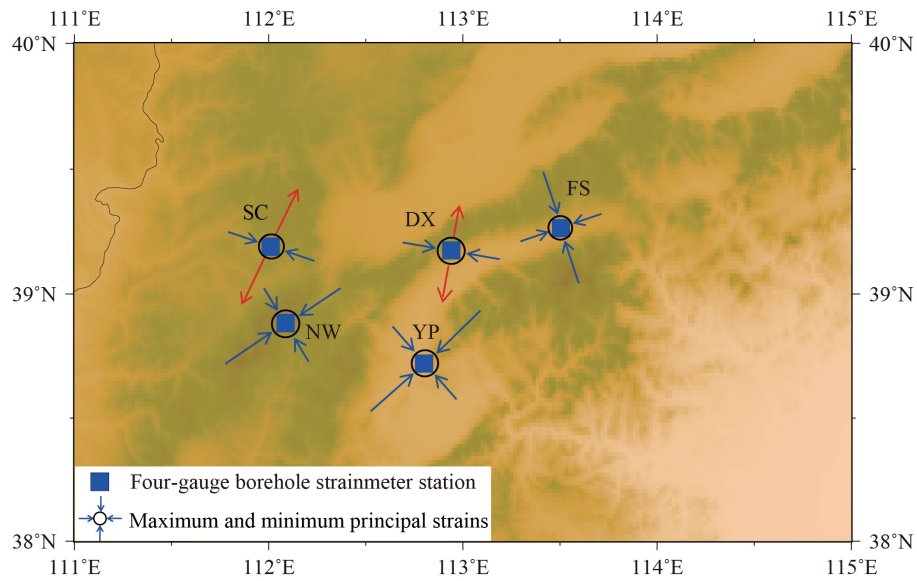


Fig. 2. (Color) Stress–strain state of the study area obtained from the FGBS observations. Red arrows represent tension, and blue arrows represent compression.

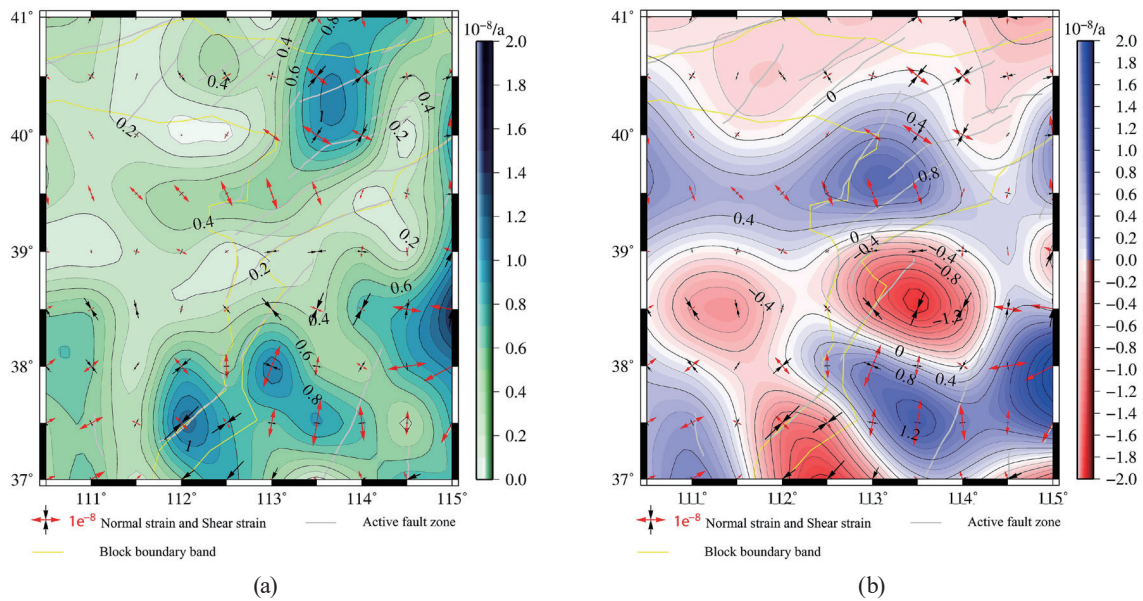


Fig. 3. (Color) (a) Maximum shear strain rate and (b) plane strain rate in the study area.

3.4 Comparison

By comparing the principal strains obtained from the two types of observation data, we found that the study area was in a stable compressive state, and the consistency between the two datasets was good. However, the amplitudes obtained from the borehole observations were larger than those obtained from the GNSS observations. This may be because the borehole strain gauge observations were for the near-surface strain (depths of about 40–60 m), whereas the GNSS observations were for the surface strain. Under the condition of a homogeneous stratum, the crustal stress and strain increase with increasing depth. Thus, the above finding is reasonable. In addition, the strain rate calculated from the borehole observations was based on the theoretical solid tide and did not consider the influence of factors such as the topography, lithology, and elevation, which may also explain why the results for the borehole strain were larger. Finally, although the results obtained from the two types of observations show that the study area was in a compressive state, there were some differences in the direction of the principal compressive strain (Fig. 4).

4. Discussion

Owing to the influences of the sensor burial depth, type of observation data, temperature, and humidity, the strain results calculated from the observations of the YRY-4 FGBS and GNSS receivers contained uncertainty, ambiguity, asynchrony, and randomness. Using the information fusion technique, we conducted a joint analysis of the strain variations using the FGBS and GNSS observations. The results comprehensively reflect the strain variations in a region, reduce the influence of the noise, and improve the reliability of the data.

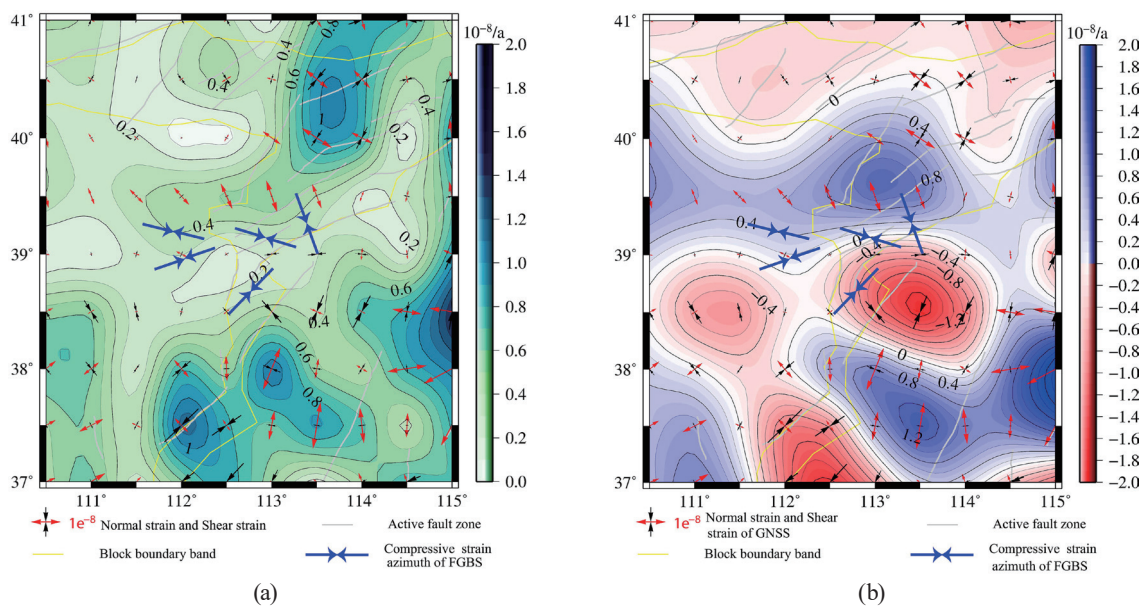


Fig. 4. (Color) GNSS and borehole stress–strain states. (a) Maximum shear strain rate and azimuth of the main direction. (b) Areal strain rate and azimuth of the main direction.

We spatially and temporally registered the two types of observation data before the joint analysis. In the spatial registration, the small-area strain calculated using the GNSS observation points around the FGBS was taken at the point with the same latitude and longitude as the FGBS. Taking the DX station as an example, Fig. 5 shows the FGBS station and the corresponding small area of the GNSS receivers. In terms of temporal registration, since the sampling frequencies of the FGBS and GNSS receivers were different, it was difficult to obtain synchronous observations from the two types of sensors. Thus, the sampling frequencies of the two sensors were synchronized. The GNSS observations were recorded in Universal Time, and the strain data were recorded in days. However, the strain data from the borehole strain gauges were recorded in hours. The least squares method is often used to normalize the sampling rate. Thus, we used this method to synchronize the principal strain results. After the spatial and temporal registration processes, the data for overlapping measuring points were fused, and the data for other points were interpolated. Then, new regional plane strain rate and maximum shear strain rate maps were generated on the basis of the fused data to reflect the regional changes in the strain.

The principal strain from the FGBS results was divided into a high-frequency part and a low-frequency part (Fig. 6). The high-frequency part had the same order of magnitude as the strain from the GNSS observations; however, there was a phase difference. For the low-frequency part, there were large differences compared with the GNSS results, which may have been caused by factors such as the water level and air pressure. Thus, the low-frequency part was excluded from the joint analysis.

On the basis of optimal estimation theory, we took the weighted average of the error covariance matrix of the GNSS principal strain and the background error covariance matrix of the FGBS as the background error covariance matrix.⁽¹⁹⁾ According to the minimum variance

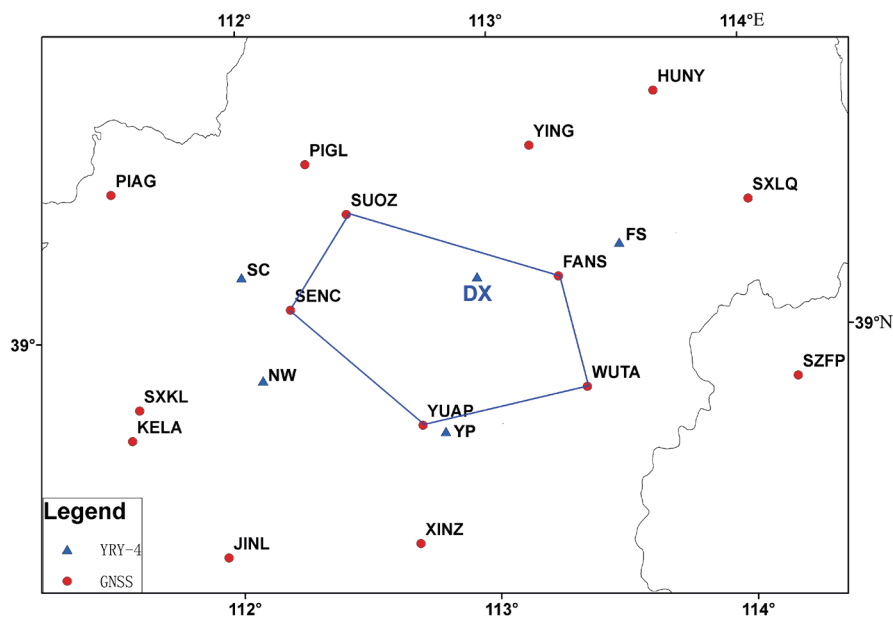


Fig. 5. (Color online) GNSS small-area observation results and FGBS results.

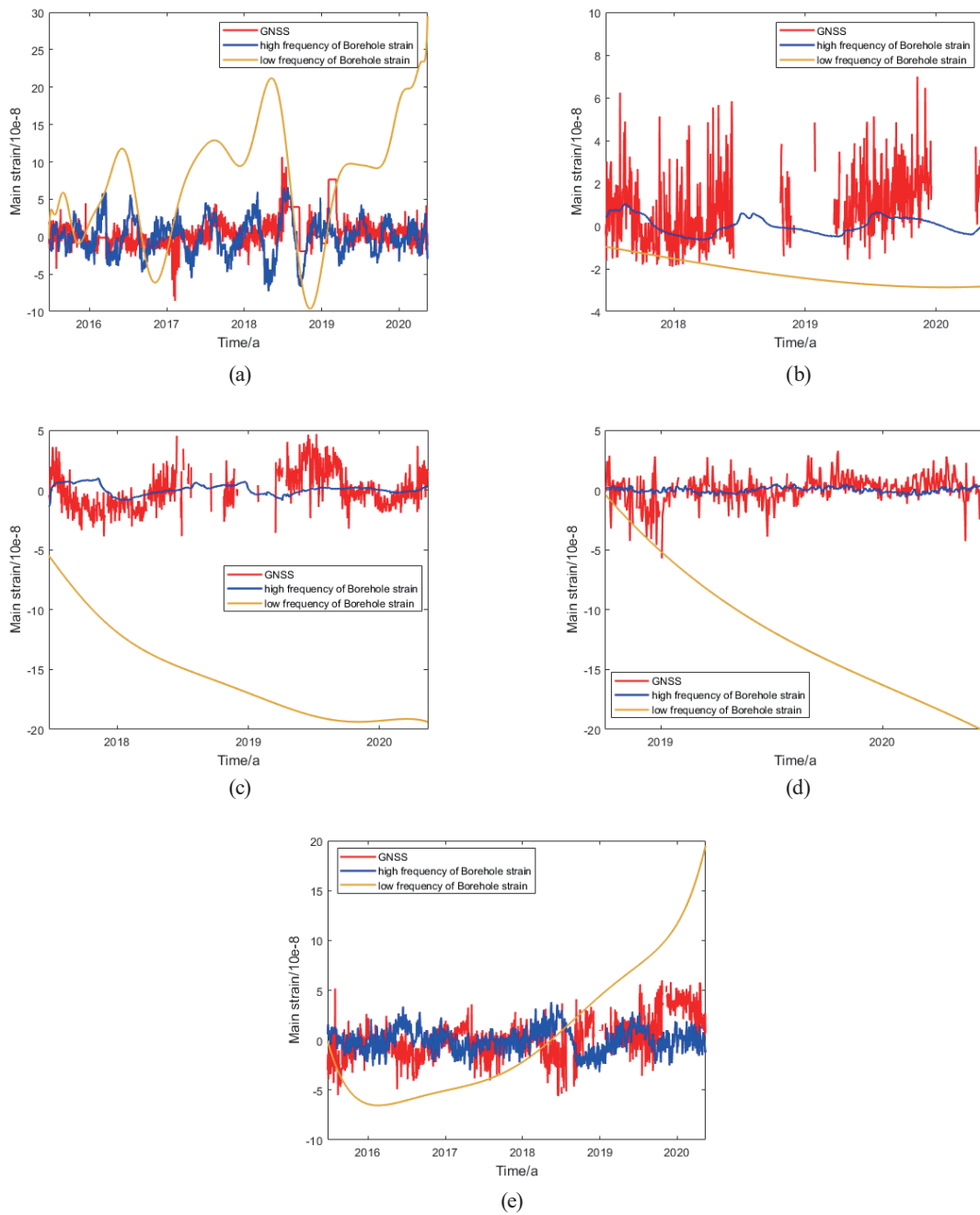


Fig. 6. (Color) Different frequency parts of observations after registration: (a) DX, (b) YP, (c) NW, (d) FS, and (e) SC.

criterion, the analytical value was closest to the real state and comprehensively reflected the strain variation in the entire region. After the data registration and fusion, the principal strain data obtained from the two types of sensors at different positions and depths were fused using the Kalman filter, which reduced the influence of the noise. The corrected FGBS, GNSS, and joint analysis results are shown in Table 2. Figure 7 shows contours obtained from joint analysis

Table 2
Results of joint analysis.

Station	Maximum shear strain rate ($10^{-8}/a$)				Plane strain rate ($10^{-8}/a$)			
	Corrected FGBS	GNSS	Joint analysis	RMSE after fusion	Corrected FGBS	GNSS	Joint analysis	RMSE after fusion
DX	0.02	0.24	0.09	0.25	0.01	0.18	0.07	0.17
YP	0.01	0.77	0.37	0.09	0.01	0.77	0.28	0.19
NW	0.03	0.42	0.18	0.21	0.22	0.42	0.16	0.21
FS	0.05	1.16	0.41	0.33	0.02	0.64	0.24	0.07
SC	0.02	0.16	0.08	0.24	1.60	0.84	0.27	0.24

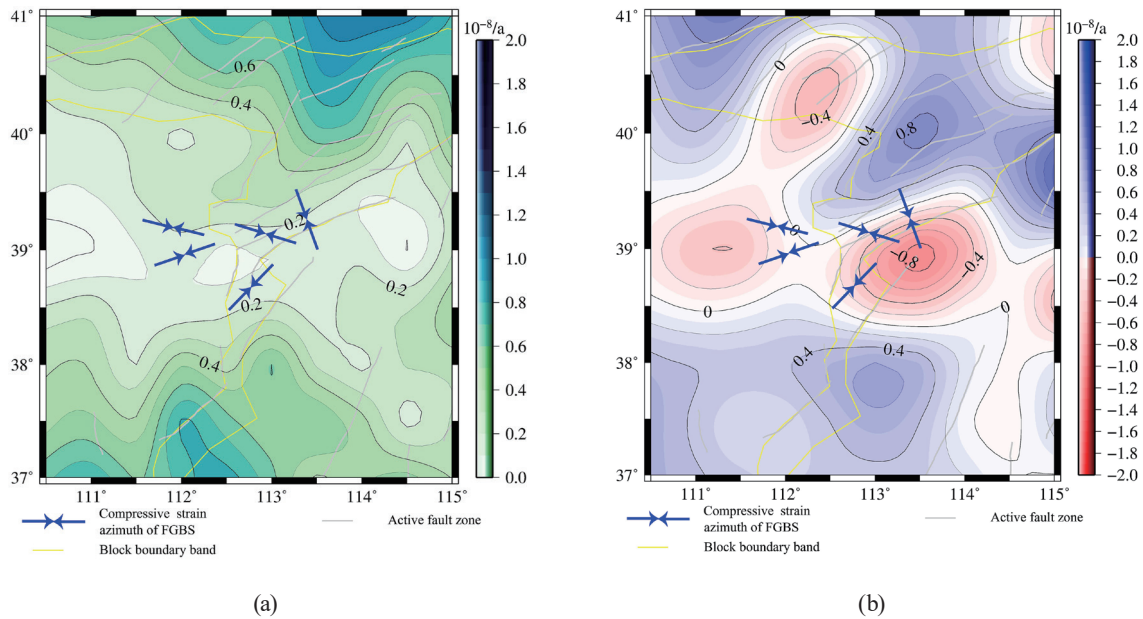


Fig. 7. (Color) (a) Maximum shear strain obtained from joint analysis and (b) plane obtained from joint analysis.

of the regional strain change, with the principal compressive strain direction of the FGBS superimposed. It can be seen that the contours of the strain change are consistent with the compressive strain direction of the FGBS. The results indicate that the proposed method is feasible and that the fused data comprehensively and intuitively reflect the overall strain variations in the study area. It was concluded that the study area is currently in a stable compressive state.

5. Conclusions

In this study, joint analysis of FGBS and GNSS observations was carried out, and the stress–strain state of the study area was analyzed from the point source scale to the regional scale and from the surface to the near surface. The results revealed the following. (1) The seismic activity level in the Xinzhou area was relatively low. The strain results obtained from the GNSS observations and the FGBSs were in good agreement. (2) The fused results obtained using the

Kalman filter reflected the deformation state of the study area. The proposed method can be used for joint analysis of these two types of observations.

The joint analysis of FGBS and GNSS observations comprehensively and intuitively yielded the deformation state of the study area. The comprehensive analysis suggests that the study area is currently in a stable compressive state. The results of this study show that the GNSS and FGBSs can be used to observe the deformation of two different sensor instruments. Arranging the two types of sensor instruments at the same station can facilitate 3D observation of the surface and shallow surface of the region. Finally, note that improvements to the proposed method are required to eliminate the phase difference and low-frequency information generated by water level and air pressure interferences.

Acknowledgments

This work was supported by the National Natural Science Foundation of China (Grant Nos. 41974018 and 42004010) and the Beijing Natural Science Foundation, China (Grant No. 8204077).

References

- 1 Z. H. Qiu, L. Tang, B. H. Zhang, and Y. P. Guo: *J. Geophys. Res.: Solid Earth* **118** (2013) 1609. <https://doi.org/10.1002/jgrb.50112>
- 2 X. Y. Liu, Z. Y. Wang, H. F. Fang, S. M. Huang, and L. Wang: *Chin. J. Geophys.* **57** (2014) 3332 (in Chinese). <https://doi.org/10.6038/cjg20141020>
- 3 P. G. Silver, Y. Bock, D. Agnew, T. Henyey, A. T. Linde, T. V. Mcevilly, J. B. Minster, B. A. Romanowicz, I. S. Sacks, R. B. Smith, S. C. Solomon, and S. A. Stein: *IRIS Newsl.* **16** (1999) 7. <http://www.iris.iris.edu/newsletter/EE.Fall98.web/plate.html>
- 4 Y. B. Wang, Y. Li, Y. Cai, L. J. Jiang, H. B. Shi, Z. S. Jiang, and W. J. Gan: *Chin. J. Geophys.-Ch.* **65** (2022) 523 (in Chinese). <https://doi.org/10.6038/cjg2022P0436>
- 5 Y. Li: *Earthquake Res. Adv.* **11** (2021) 29. <https://doi.org/10.1016/j.eqrea.2021.100028>
- 6 R. Ohtani, N. Matsumoto, K. Nawa, and S. Itaba: *Bull. Geol. Surv. Jpn.* **63** (2012) 93 (in Japanese). <https://doi.org/10.9795/bullgsj.63.93>
- 7 Z. H. Qiu, S. L. Chi, and L. Tang: *Sci. China.* **54** (2011) 1031 (in Chinese). <https://doi.org/10.1007/s11430-010-0049-4>
- 8 K. I. S. Sacks, S. Suyehiro, and D. W. Evertson: *Proc. Jpn. Acad.* **47** (1971) 70. <https://doi.org/10.2183/pjab1945.47.707>
- 9 K. Z. Su: *Seismolog. Res.* **4** (1982) 57 (in Chinese).
- 10 S. L. Chi, Y. Chi, T. Deng, C. W. Liao, X. L. Tang, and L. Chi: *Recent Dev. World Seismolog.* **1** (2009) 1 (in Chinese).
- 11 Z. X. Ouyang, Z. R. Zhang, and G. L. Shu: *Chin. J. Rock Mech. Eng.* **23** (2004) 4058 (in Chinese). <https://doi.org/10.3321/j.issn:1000-6915.2004.23.025>
- 12 M. T. Gladwin: *Rev. Sci. Instrum.* **55** (1984) 2011. <https://doi.org/10.1063/1.1137704>
- 13 Y. Q. Wu, Z. S. Jiang, G. H. Yang, Y. Fang, and W. X. Wang: *Chin. J. Geophys.-Ch.* **52** (2009) 1707 (in Chinese). <https://doi.org/10.3969/j.issn.0001-5733.2009.07.005>
- 14 G. S. El-Fiky, and T. Kato: *J. Geodyn.* **27** (1998) 213. [https://doi.org/10.1016/S0264-3707\(98\)00006-4](https://doi.org/10.1016/S0264-3707(98)00006-4)
- 15 Y. Q. Wu, Z. S. Jiang, G. H. Yang, W. X. Wei, and X. X. Liu: *Geophys. J. Int.* **185** (2021) 703. <https://doi.org/10.1111/j.1365-246X.2011.04976.x>
- 16 S. J. Whitaker and T. M. Hamill: *Mon. Weather Rev.* **130** (2002) 1913. <https://doi.org/10.1175/1520-0493130>
- 17 Z. Altamimi and A. Dermanis: *VII Hotine-Marussi Symp. Mathematical Geodesy (IAG, 2009)* 329–334.
- 18 H. Ishii: *Report of Tono Research Institute of Earthquake Science* **6** (2001) 5 (in Japanese).
- 19 X. Wang, T. M. Hamill, J. S. Whitaker, and C. H. Bishop: *Mon. Weather Rev.* **135** (2007) 1055. <https://doi.org/10.1175/MWR3307.1>